J. R. Echols, L. M. Garrison, N. Reid, C. M. Parish, D. Morrall, A. Hasegawa, A. Bhattacharya, Y. Katoh

Degradation of electrical resistivity of tungsten following shielded neutron irradiation

Degradation of electrical resistivity of tungsten following shielded neutron irradiation

J. R. Echols, L. M. Garrison, N. Reid, C. M. Parish, D. Morrall, A. Hasegawa, A. Bhattacharya, Y. Katoh

Degradation of electrical resistivity of tungsten following shielded neutron irradiation

J. R. Echols[1,2], L. M. Garrison[1], N. Reid[1,3], C. M. Parish[1], D. Morrall[1,4], A. Hasegawa[5], A. Bhattacharya[1], Y. Katoh[1]

[1]*Materials Science and Technology Division, Oak Ridge National Laboratory, Oak Ridge, TN, USA*

[2] *UK Atomic Energy Authority, Culham, England, United Kingdom*

[3]*University of Illinois Urbana Champaign, Champaign, IL, USA*

[4]*Savannah River National Laboratory, Aiken, SC, USA*

[5]*Tohoku University, Sendai, Miyagi, Japan*

Graphical Abstract
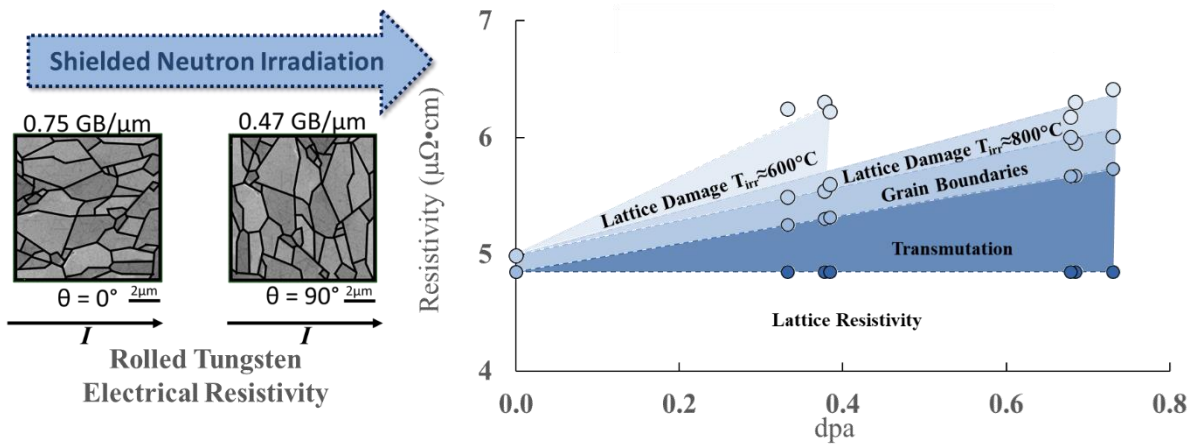
Abstract

A major challenge for heat transfer in nuclear materials is to ensure thermal mobility after high

amounts of neutron irradiation. Tungsten is widely selected as a heat transfer material in fusion

reactors. In metals, thermal conductivity is dominated by electrons' ability to transfer energy. Neutron

irradiation generates point defects, clusters, and solid transmutation (e.g.rhenium and osmium in

18 tungsten), which inhibit electron motion. The purpose of this work is to quantify the irradiation-induced

19 change in electron mobility and deconvolute transmutation and microstructural effects on observed

20 changes to electron mobility.

21 Single and polycrystalline tungsten were fast neutron irradiated in the High Flux Isotope Reactor at Oak

22 Ridge National Laboratory to doses between 0.2 and 0.7 displacements per atom (dpa) and

23 temperatures from 500°C to 1000°C. Grain growth was observed in all samples. Microstructure and

24 transmutation were quantified. The geometric orientation of samples with elongated grains has been

25 shown to affect electrical resistivity. A mathematical model was developed and used to deconvolute

26 solid-solution transmutation, grain, and temperature-dependent lattice effects on resistivity. At ~0.4

27 dpa at ~590°C, the combined resistivity degradation due to voids, vacancies, interstitials, and

28 dislocations is estimated to be greater than the contribution from solid solution Re transmutation, which

29 is greater than the contribution from grain boundaries. At doses of ~0.7 dpa at ~750°C, solid solution Re

30 contributions are greater than all other effects combined. This work establishes a basis to predict the

31 effects of irradiation temperature and transmutation on thermal properties of tungsten and highlights

32 the importance of irradiation temperature.

33 # 1 Motivation and Introduction

34 Development of fusion power plants faces the technical obstacles of effective plasma containment and

35 survivable materials. The challenge of materials, in deuterium-tritium fusion, is dominated by a high

36 fluence of 14.1 MeV neutrons, which provide significant damage to the first wall of materials the

37 neutrons encounter following the fusion reaction. The divertor of a tokamak power plant, which

38 captures and transfers the heat of the reaction, is expected to be subject to 20-30 displacements per

39 atom (dpa) of neutron damage over a reactor lifetime[1]. Radiation-induced defects and transmutation

40 will degrade the thermal conductivity of the divertor materials, which can severely impact the

41 components' ability to effectively remove heat produced in the fusion reactor.

42

43   The thermal conductivity of metals depends primarily on the motion of electrons and phonons but

44   becomes less efficient due to scattering of electrons and phonons. The electronic contribution to the

45   thermal conductivity, κ_e, is dominant in metals and often approximated by the Wiedemann–Franz law:

46   *Equation 1:*

47    $$\frac{\kappa_e}{\sigma} = LT$$

48   Where σ is electrical conductivity, T is temperature, L is the Lorenz number. The actual proportionality

49   factor L deviates from the theoretical Lorenz number depending on temperature and material.

50   Tungsten or its alloys are the presumptive material for the divertor- the heat removal component - in

51   many paths for fusion [1,2]. Tungsten possesses an unusually high L, typically reported as $3.2 \bullet 10^{-8}$

52    $W\Omega K^{-2}$ [3] where W is Watts, Ω is Ohms, and K is degrees Kelvin. There is disagreement in the literature

53   as to the extent of the phononic contribution to the thermal conductivity of tungsten[3–7], with the

54   estimated ranges between 25%[3,7] to less than 1%[8] of the total thermal conductivity. The majority of

55   literature on tungsten, however, assumes negligible phonon contribution[9,10]. The motion of

56   electrons, therefore, is expected to dominate the material's ability to transfer heat both prior to and

57   following irradiation. Therefore, we measured electrical resistivity to provide direct insight to the

58   degradation of the electron transport.

59

60   Resistivity degradation measurements in lattice-damaged and/or transmuted tungsten exist mainly in

61   the context of determining the temperature effects on lattice recovery [11–14]; e.g. temperatures

62   where vacancy mobility becomes high enough to annihilate significant Frenkel-pairs on small timescales.

63   Only limited work exists on neutron irradiated changes to resistivity at neutron dose levels above 0.1

64   dpa [15–17]. A more complete understanding of the changes to electron mobility in fusion-relevant

65   tungsten irradiation is necessary. This understanding not only allows us to evaluate whether the

66   Wiedemann–Franz law holds under irradiation, but also impacts component lifetime and design criteria,

67   and has the potential to reveal design spaces for optimizing tungsten and tungsten alloy thermal

68   properties for fusion-relevant radiation damage. Here, fusion-relevant neutron spectrums are defined

69   as having a higher fast neutron to thermal neutron ratio than what is generated in reactors such as the

70   High Flux Isotope Reactor (HFIR). This allows more accurate simulation of neutron damage for fusion

71   scenarios which will be dominated by 14.1 MeV neutrons.

72

73   The Plasma Facing Component Evaluation by Tritium, Plasma, Heat, and Neutron Irradiation

74   Experiments (PHENIX) project [18] presents an ideal opportunity to evaluate electrical resistivity of

75   irradiated tungsten microstructures and alloys. PHENIX is the latest in a series of U.S.-Japan

76   collaborations for the technological assessment of plasma facing components for demonstration power

77   plants. One of the main goals of this experiment is to understand the thermomechanical properties of

78   tungsten irradiated with a transmutation-to-dpa ratio relevant to fusion plasma facing components

79   (PFCs), which is accomplished through the use of an irradiation shield made of gadolinium [18].

80

81   Two key, quantifiable factors to determining electron mobility following irradiation are 1) the amount

82   and distribution of transmutation that has occurred (W to Re and Re to Os) and 2) microstructural

83   changes to the lattice including defects and any larger-scale microstructural evolution.   By measuring

84   the electrical resistivity of unirradiated/irradiated tungsten with varying levels of transmutation and

85   thermal recovery some decoupling of these factors can be achieved. Therefore, the purpose of this

86   work is the following:

87   • Test the Wiedemann–Franz law in neutron irradiated tungsten

88   • Deconvolute and determine the transmutation and grain boundary effects on electronic

89   conductivity in tungsten.

90

2 Methods and Materials

2.1 Materials

93 A variety of single-crystal and polycrystalline tungsten/tungsten alloy samples were irradiated in the

94 PHENIX campaign[19,20]. The materials which were selected for resistivity testing are summarized in

95 Table 1. The selected materials include commercial varieties of single and polycrystalline tungsten (SCW

96 and PCW, respectively), a variety of grain sizes/elongation, and three samples with Re or Re+K as

97 alloying elements to W. W-Re alloys are under consideration as a more-ductile alternative to pure W

98 and have the added benefit of approximating transmutation conditions of higher doses than actually

99 experienced. K-doped W-Re has the potential to improve tensile and creep strength. Figure 1 shows

100 SEM images of a subset of samples which were cut from the same parent block of material in 3 different

101 directions. Although the material arrived with no indication of the longitudinal (L), short transverse (S),

102 and long transverse (T) directions, reasonable assumptions can be made as to these directions from the

103 SEM images. The assumed planes are also indicated in Figure 1 and Table 1.

104 Prior to irradiation, samples were machined into 3mm diameter by 0.5mm thick disks, first by cutting

105 with electrical discharge machining, then by grinding/polishing to an 800 grit finish to remove

106 contamination and artifacts from the cutting process. The SCW material was more sensitive to

107 machining defects, so the cut surface had to be ground and polished deeper than the PCW to produce a

108 surface more representative of the bulk material. Finally, samples were engraved with a material

109 specific, two symbol code and sample numbers.

Material Code	Description	Manufacturer	W (at%)	Re (at%)	K (ppm)
AT	PCW w/ sample face in the T x S plane	ALMT	99.998	-	-
BT	PCW w/ sample face in the L x T plane	ALMT	99.998	-	-
CT	PCW w/ sample face in the L x S plane	ALMT	99.998	-	-
UE	SCW w/ surface plane (110)	Goodfellow	99.999	-	-
41	W-3%Re, rolled 80%	ALMT	97	3	-
70	K-doped W-3%Re, rolled 80%, recrystallized at 1500°C	ALMT	97	3	28
80	K-doped W-3%Re, rolled 80%	ALMT	97	3	28

T x S Plane (AT) L x T Plane (BT) L x S Plane (CT)
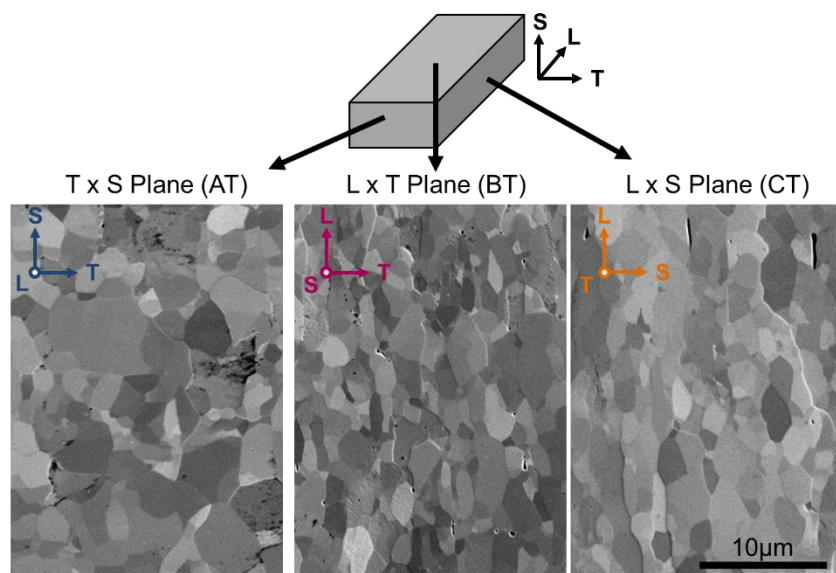
Figure 1. Microstructure of and relationship to rolling direction for PCW samples. Relationships between the longitudinal (L), short transverse (S), and long transverse (T) directions are indicated.

2.2 Irradiation Conditions

The HFIR at Oak Ridge National Laboratory (ORNL) provides a high flux of neutrons, allowing for rapid turnaround materials testing. However, the reactor has a much higher flux of thermal neutrons than

121   what is expected in future fusion reactors [21,22]. The capsule irradiated in this campaign, RB-19J, was

122   designed to limit thermal neutron exposure by utilizing a thermal shield made of Gd metal surrounding

123   the specimen regions. The thermal flux is expected to be reduced by 1.5-2 orders of magnitude

124   compared to HFIR's normal spectrum [23]. The intended effect from this is to achieve a thermal-to-fast

125   neutron ratio more similar to a fusion spectrum. One important change from this is the reduction of

126   the tungsten transmutation-to-dpa ratio from as high as 50:1 (at%) to nearly 1:1 [23,24]. Figure 2 shows

127   a direct comparison the transmutation-to-dpa ratio for RB-19J alongside upper and lower estimations of

128   fusion-reactor transmutation calculated from Noda[25] and Sawan[26], respectively. Full information on

129   the design of the capsule is documented in [27].

130   The divertor will experience an incredibly wide operational temperature window between the plasma-

131   facing side and the coolant side. Several steady state designs require temperatures more than 2000°C at

132   the plasma facing side, dropping to several hundred degrees on the coolant side[28,29]. Therefore, the

133   PHENIX project was designed to test W at three different fusion-relevant temperature regions which are

134   approximated as the 500°C, 800°C, and 1200°C. The RB-19J capsule had three sub-capsules, each

135   designed for one of these temperatures, and over 1300 samples were ultimately irradiated.

136
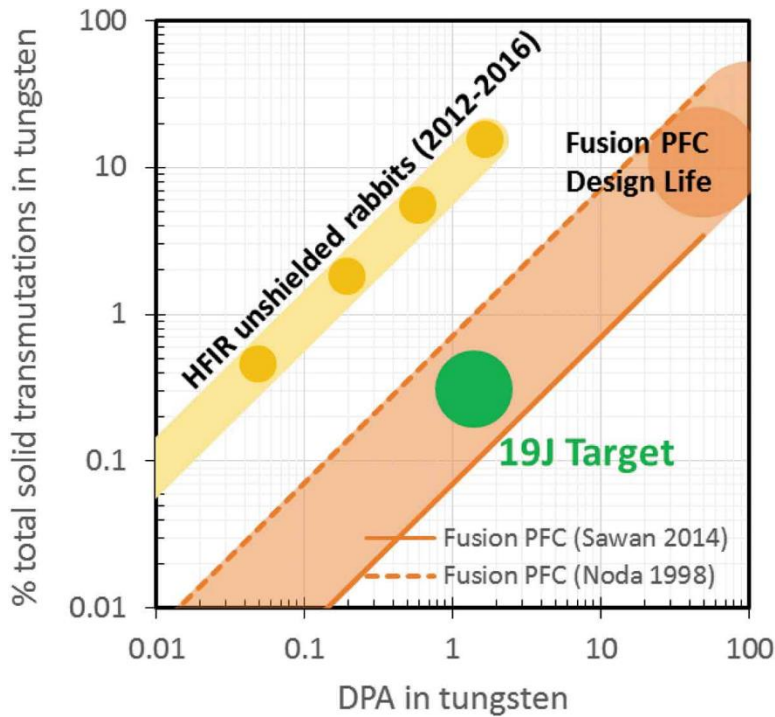
Figure 2. Expected irradiation profile from the 19-J capsule [23].

138   Specimens evaluated here experienced a calculated irradiation temperature range of 550°C to 1000°C

139   with calculated DPA values ranging from 0.30 to 0.71. DPA was calculated based on the work of Sawan

140   [26] from fast neutron flux. This flux was estimated by an in-house HFIR code which has been shown to

141   accurately predict neutron flux with 87%-99.5% accuracy [30]. Irradiation occurred over the course of 4

142   cycles (average cycle length of 24.5 days) in HFIR The irradiation temperature and DPA of each sample is

143   shown with their results in Table 2.

144   Temperatures in the irradiation capsules were calculated with a combination of active thermocouple

145   measurement (monitored during irradiation at discrete locations), passive SiC thermometry (determined

146   following irradiation[31]), and thermal modelling of the RB-19J capsule. In the highest temperature

147   subcapsule, failure of thermocouples midway through irradiation resulted in greater temperature

148   uncertainty for those samples. Out of an abundance of caution, these samples' temperatures are listed

149   with an uncertainty of ±100°C based on best practices developed in earlier campaigns and noted in the

150   results section.

2.3   Reaction Layer Removal

152   A thin reaction layer was discovered on some samples irradiated at higher temperatures. The samples

153   were in graphite holders and had thin graphite spacers between each sample during irradiation. All

154   components and samples were cleaned with alcohols prior to irradiation and mixes of high purity Ar and

155   He were used as the fill gas in the capsule. Scanning electron microscopy (SEM) and energy-dispersive x-

156   ray spectroscopy (EDS) of this layer suggest oxide and/or carbide formation on the sample surfaces to a

157   maximum observed depth of 50 µm, as seen in Supplemental Figure 1. To avoid measuring the

158   combined resistivity of the film and bulk, samples from the two higher temperature capsules were

159   lightly polished on the lead contact side prior to testing (See Supplemental Figure 1). The final thickness

160   after polishing was used to calculate resistivity and the resistivity testing device was confirmed to give

161   accurate resistivity regardless of sample thickness on unirradiated tungsten.

2.4   Resistivity testing

163   Nondestructive, miniaturized resistivity testing equipment was designed and implemented at ORNL for

164   3mm diameter x 0.5mm thick samples. Figure 3 shows a diagram of the resistivity tester developed for

165   this work. The sample is held steady by a clamp in a non-conductive fixture the contacts are small round

166   points of copper touching the surface of the sample. The device passes a current across the material

167   and measures the voltage drop over a known length.

168
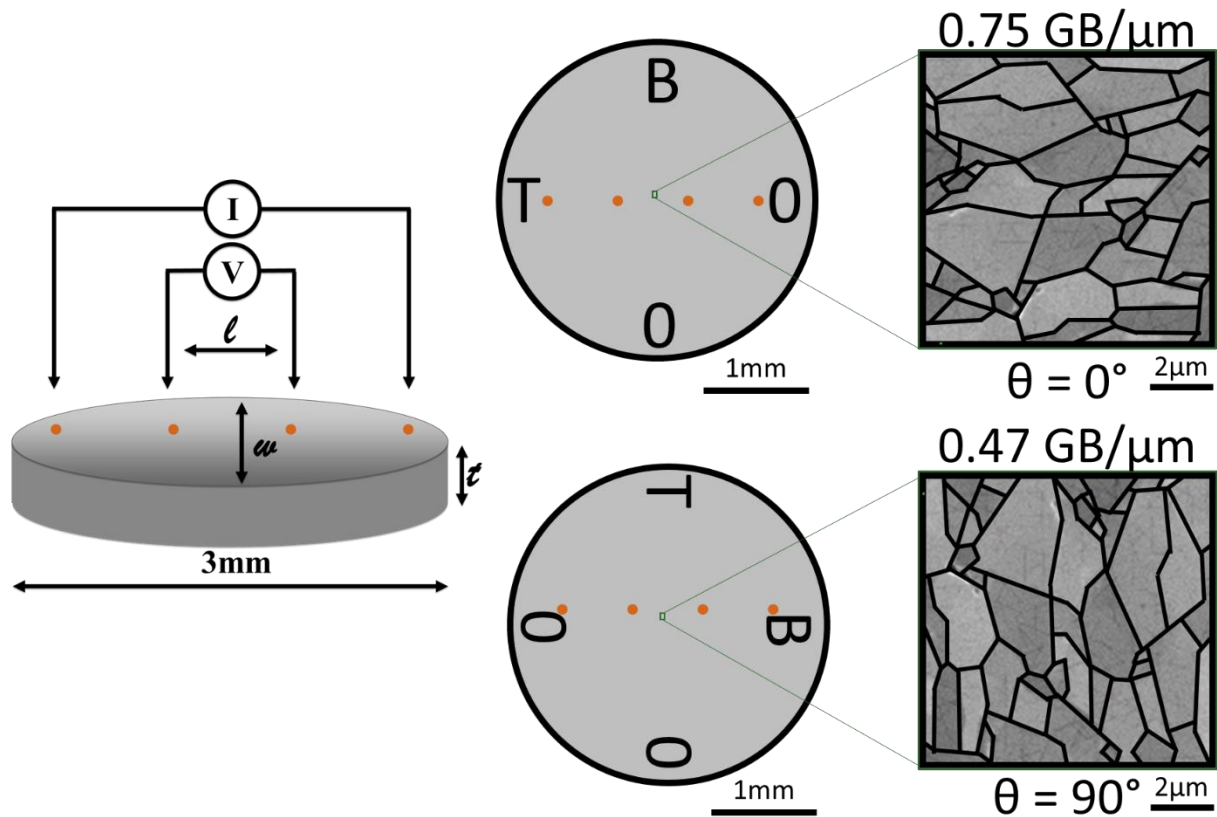
Figure 3. Schematic of resistivity measuring apparatus with copper contact locations shown in orange. Rotating a sample with

elongated grains changes the GB density in the direction of the current flow. The grains on the right of the image are one

example taken from a sample, but simplified as a drawing to illustrate how the rotation of the sample in the fixture changes

how the grains are oriented relative to the measurement probes.

The resistivity of the measured material is dependent on upon the geometry tested. For the 3mm disk

tester, the relationship is as follows [32]:

Equation 2:

$$\rho = \frac{V}{I} \cdot t \cdot C.F.$$

Here again, ρ is the resistivity, V is the measured voltage drop across the middle two probes, I is the

current passed through the sample from the outer two probes, t is the minimum measured sample

178   thickness, and C.F. is a conversion factor calculated from the length and width of the individual samples

179   in a process described fully by Logan [32]. For a circular sheet sample with insulated edges, C.F. is

180   calculated as:

181   *Equation 3:*

182
$$C.F. = \frac{\pi}{\ln(2) + \frac{1}{2}\ln\left(\frac{\left[1 - \left(\frac{2a}{d} + \frac{S}{d}\right)\left(\frac{2a}{d} - \frac{3S}{d}\right)\right]\left[1 - \left(\frac{2a}{d} - \frac{S}{d}\right)\left(\frac{2a}{d} + \frac{3S}{d}\right)\right]}{\left[1 - \left(\frac{2a}{d} - \frac{S}{d}\right)\left(\frac{2a}{d} - \frac{3S}{d}\right)\right]\left[1 - \left(\frac{2a}{d} + \frac{S}{d}\right)\left(\frac{2a}{d} + \frac{3S}{d}\right)\right]}\right)}$$

183   Where d is the diameter of the measured disk, S is the distance between each probe (0.61 mm in our

184   custom fixture), and a is the distance between the center-point of the 4-probe system and the center

185   point of the disk. In this case, a is 0, which simplifies the expression to:

186   *Equation 4:*

187
$$C.F. = \frac{\pi}{\ln(2) + \frac{1}{2}\ln\left(\frac{\left[1 + \left(\frac{S}{d}\right)\left(\frac{3S}{d}\right)\right]^2}{\left[1 - \left(\frac{S}{d}\right)\left(\frac{3S}{d}\right)\right]^2}\right)}$$

188   Because the diameter of each sample differed slightly, this conversion factor was calculated separately

189   for each sample. Sample diameter and thickness were measured thrice with a micrometer, and

190   averaged for resistivity calculation. Voltage measurements were performed on a Keithley Model 182

191   Sensitive Digital Voltmeter. The current source was provided with a Keithley Model 237 High Voltage

192   Source Measure Unit. Resistivity testing was performed between 20°C and 24°C with a minimum of 5

193   (15 max) measurements performed on each sample or each rotation condition. Samples which were

194   rotated had measurements taken at 45° intervals. Resistivity values were then normalized to 20°C for

195   accurate comparison. General test procedures for electrical resistivity testing on metals are given in

196   ASTM B 193-20, Standard Test Method for Resistivity of Electrical Conductor Materials[33].

2.5 Thermal Diffusivity

Thermal diffusivity measurements were performed on irradiated and unirradiated SCW samples using a xenon flash and following the procedures from [34] (where PCW results are reported), including the use of graphene spray sold as 'JA007159: Black coating agent for LFA on very thin specimen' from NETZSCH Japan. While the electrical resistivity measurements are performed with the current passing parallel to the disk surface, the thermal diffusivity instrument measures in the perpendicular direction, which is through the thickness of the sample. A NETZSCH LFA-467 HT was used to for the thermal diffusivity measurements. The device was evacuated to $<4 \times 10^{-4}$ Torr, and measurements were taken between room temperature and up to 800°C, depending on the maximum irradiation temperature.

2.6 Microscopy

Electron and Electron Backscatter Diffraction (EBSD) micrographs were taken on a TESCAN MIRA3 Scanning Electron Microscope (SEM) with an advanced Oxford Symmetry EBSD system. Compositional analyses were acquired on an electron microprobe (JEOL 8200) equipped with 5 tunable wavelength dispersive spectrometers. The accelerating voltage was set to 25.0 kV and the beam current was 50.0 nA. Elements were acquired using LiF analyzing crystals for W lα, Re lα, and Os lα. Pure standards were used to calibrate all elements except for Os for which the average intensities of Re lα and Ir lα were used to create a virtual standard. Unknown and standard intensities were corrected for deadtime. Standard intensities were corrected for standard drift measured between the beginning and end of the run. Interference corrections were applied to Re for interference by W and both W and Re for Os.

3   Results

3.1   Microstructure and composition

3.1.1   Grain Structure

EBSD micrographs for the three sample orientations are shown in Figure 4 (with statistics in Table 2), alongside L x S orientation samples from three irradiation conditions. A single-pass cleaning procedure was performed on the EBSD data (using the OIM Analysis software by EDAX) to generate accurate grain size measurements in the data and is reflected in the images in the figure. Grain diameters and areas are shown for all measured samples in Table 2. Recrystallization and grain growth are observed in the 990°C, 0.71 dpa specimen. Visually, the 550°C, 0.29 dpa and 870°C, 0.70 dpa specimens' grains look the same as the unirradiated sample. To statistically try to determine if grain growth occurred between the irradiation conditions, a 2-sample Kolmogorov-Smirnov test was performed on the grain areas to determine if the populations could be considered identical. Results of this test can be seen in Table 3.

The p-values for all tests indicate that we can reject the null hypothesis and conclude that all populations of grain area are distinct. Quantifiable grain growth has occurred at all irradiation conditions. For the lower temperatures, we believe this is most likely irradiation-induced. In the highest temperature irradiation, we observe large growth and/or recrystallization - likely well below what we would expect for unirradiated annealing for this irradiation length [35]. Practically, we consider grain distributions similar for irradiations below 870°C. Large amounts of recrystallization and/or grain growth is only considered for samples irradiated at temperatures >870°C. Histograms comparing the grain sizes are shown in Supplemental Figure 1. Based on the results of the CT samples, we postulate that the AT and BT samples may also have had minimal grain growth for irradiation temperatures <870°C, and potentially recrystallized at higher irradiation temps. We discuss the resistivity results with that in mind.

240
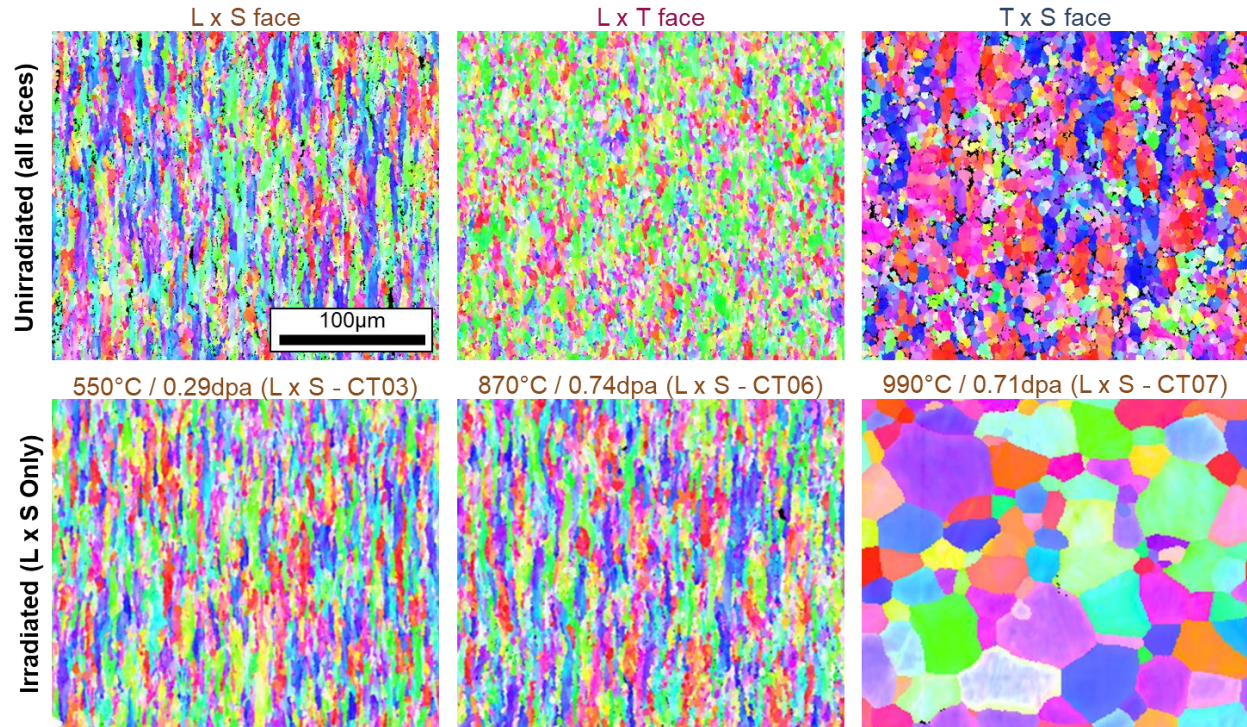
Figure 4. Inverted Pole Figure maps (z-direction) of unirradiated (top) and irradiated (middle) PCW samples. Histograms of grain area are shown for irradiated specimens in Supplemental Figure 2, indicating minor grain growth below the highest temperature irradiation.

Table 2. Grain sizes and irradiation conditions for selected specimens from EBSD data shown in Figure 4.

Sample Face (ID)	Irradiation Temp (°C)	Dose (dpa)	N Grains	Mean Area (μm^2)	Mean Maj Diameter (μm)	Mean min Diameter (μm)
T x S (AT no rad)	-	0	12209	18.2	2.1*	2.1*
L x T (BT no rad)	-	0	14930	5.6	1.7	0.8
L x S (CT no rad)	-	0	32853	7.1	2.0	0.8
L x S (CT03)	550	0.29	27633	7.6	2.2	0.8
L x S (CT06)	870	0.74	26072	8.3	2.2	0.9
L x S (CT07)	990	0.71	2466	345	11.9*	11.9*
SCW (UE06)	990	0.70	-	-	-	-

*Equiaxed grains on average

Table 3. Kolmogorov-Smirnov test results with associated p-values for the grain area of representative samples.

	550°C, 0.29 dpa (CT03)	870°C, 0.70 dpa (CT06)	990°C, 0.7dpa (CT07)
No irradiation	0.07 p=10^{-58}	0.15 p=10^{-272}	0.90 p=0
550°C, 0.29 dpa (CT03)	-	0.09 p=10^{-98}	0.90 p=0
870°C, 0.70 dpa (CT06)	-	-	0.89 p=0

247

248 Measurements of the angular dependence of resistivity for six specimens are shown in Figure 5.

249 Unirradiated and irradiated B-series PCW (which does not have equiaxed grains relative to the current

250 for different rotations in the resistivity fixture) show resistivity that oscillates with measurement angle.

251 However, samples which are likely recrystallized (BT08), equiaxed relative to the current (AT01) or have

252 no grains (UE06), do not oscillate, meaning the oscillatory behavior results from the effects of grain

253 boundaries (GBs), rather than textural effects. Sine curves fits to the oscillatory data and the amplitude

254 in oscillations might be taken as the GB effect on resistivity.
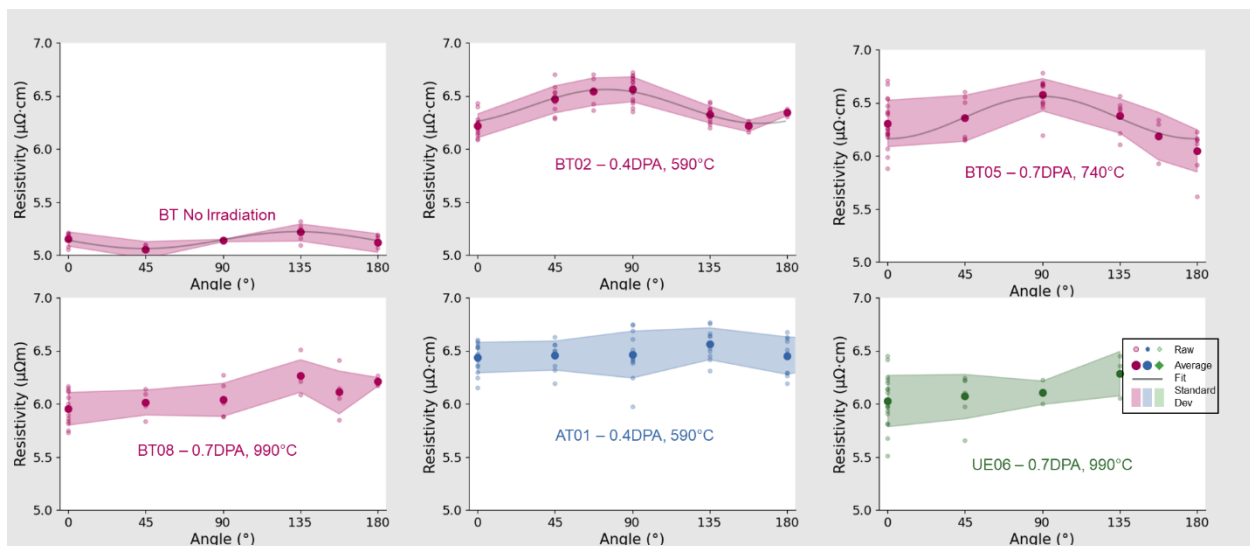
256 *Figure 5. Resistivity as a function of sample rotation in the fixture during measurement. Fit lines are shown for the top row of*

257 *samples, which behave in a periodic fashion. Samples shown in the bottom row do not exhibit periodicity. The starting angle,*

258 *0°, was arbitrary and therefore not consistent across samples.*

259 3.1.2   Elemental Composition

260 Composition was measured by Wavelength-Dispersive Spectroscopy (WDS) for samples of SCW, PCW,

261 irradiated W-Re alloys, and unirradiated W-Re-Os alloys (Table 4). Unirradiated W-Re alloys were

262 measured by inductively coupled plasma - optical emission spectrometry (ICP-OES) by Evans Analytical

263 Group.

264   Elemental composition samples are distinct from those from which the resistivity measurements were

265   taken. For the WDS samples, 10 distinct sites in the bulk of each sample were measured, and the

266   average transmutation levels are shown alongside a single standard deviation. For the unalloyed

267   samples, EDS maps taken during measurement do not show any resolvable areas of Re/Os

268   concentration, and we assume relatively uniform distribution of transmutant elements at WDS-relevant

269   scales (note that segregations such as nanoscale clusters of Re and Os observed in [36] and grain

270   boundary segregation observed in [37] would not show up in the larger areas considered by WDS) [36].

271   For unalloyed specimens, if we also assume linear transmutation rates in this dose regime[10], we

272   calculate a dose-: transmutation ratio of 1 dpa : 0.83 Re (at %). The R^2 value of our data to this fit is 0.98,

273   giving confidence in this assumption. Pre-alloyed specimens are not expected to exhibit the same

274   transmutation ratio since Re continues to transmute to Os.

275   *Table 4. Elemental composition of selected samples measured by WDS. Error represents a single standard deviation in either*
276   *direction.*

Sample Type	Sample ID	Irradiation Temp (°C)	Dose (dpa)	Measured Re (at%)	Measured Os (at%)
PCW	AT00	510	0.33	0.23 ± 0.03	0.00 ± 0.00
	AT08	780	0.69	0.57 ± 0.02	0.00 ± 0.01
	AT0G	900	0.66	0.50 ± 0.01	0.00 ± 0.00
SCW	UE03	480	0.26	0.16 ± 0.02	0.00 ± 0.00
	UE0A	830	0.74	0.73 ± 0.02	0.00 ± 0.00
	UE0L	930	0.63	0.49 ± 0.02	0.01 ± 0.01
W-Re Alloy	5Enorad	-	-	2.21 ± 0.02*	-
	5E00	530	0.27	2.32 ± 0.06	0.10 ± 0.02
	5E01	910	0.74	2.48 ± 0.13	0.30 ± 0.02
	3Rnorad	-	-	0.40 ± 0.01*	-
	3R01	530	0.28	0.51 ± 0.01	0.00 ± 0.00
W-Re-Os Alloy	W 3Re 0.7Os	-	-	3.07 ± 0.0	0.69 ± 0.0
	W 5Re 3Os	-	-	5.35 ± 0.0	3.67 ± 0.0
	W 10Re 5Os	-	-	10.15 ± 0.08	5.35 ± 0.03

277   ** Denotes samples measured with ICP-OES. All other measurements are measured with WDS.*

3.2 Resistivity

Measured resistivities and the calculated electronic contribution to the thermal diffusivity, α_e, along with irradiation temperature and dose, are shown in Table 5. For each sample and sample rotation condition, at least 5 measurements were taken, with the average resistivity value and standard deviation reported. Values for α_e were calculated from the Wiedemann–Franz law, assuming negligible effects from density and specific heat capacity changes in irradiated materials and a Lorenz number of $3.2 \cdot 10^{-8}$ WΩK^{-2}. Samples are color coded by material in the table and some following figures, with A-orientation PCW in blue, B-orientation in pink, and SCW in green. This data, except for the alloy samples, is visualized in Figure 6 where resistivity is shown against dose for SCW and 2 PCW grain elongation states. Irradiation temperature, which can anneal out lattice defects, is shown with a colorbar and callouts. Notably, the spread in the data for SCW samples is much larger than for the PCW. This is attributed to machining artefacts from EDM, which were much more severe on the SCW than the PCW samples and may not have been completely removed during polishing (see figure 2 in [38]) – leading to an increased apparent resistivity and variability.

Table 5. Irradiation parameters, resistivity, and calculated electronic contribution to the thermal diffusivity (α_e) of selected samples for 20°C. Re percentages are calculated from the WDS data.

Face orientation/ description	Sample ID	Irradiation Temp (°C)	Dose (dpa)	Calculated Re (at. %)	Average Resistivity ($\mu\Omega{\cdot}cm$)	STDEV ($\mu\Omega{\cdot}cm$)	α_e (mm^2/s)
T x S / PCW	AT01	590	0.38	0.32	6.30	0.18	56.2
	AT02	550	0.33	0.27	6.25	0.31	57.1
	AT04	830	0.73	0.61	6.41	0.18	55.7
	AT05	760	0.68	0.56	6.30	0.02	57.5
	AT06	990*	0.70	0.58	5.73	0.17	61.1
	AT07	990*	0.70	0.58	6.39	0.09	56.7
L x T / PCW	BTnorad	-	0.00	0.00	5.05	0.07	70.6
	BT02	590	0.38	0.32	6.22	0.11	56.7
	BT05	740	0.68	0.56	5.95	0.19	56.8
	BT06	850	0.73	0.61	6.74	0.04	53.8
	BT08	990*	0.71	0.59	5.96	0.15	59.0
L x S / PCW	CT07	980*	0.71	0.59	6.63	0.03	54.6
SCW	UEnorad	-	0.00	0.00	4.85	0.08	74.7
	UE02	550	0.30	0.25	5.49	0.41	66.0

	UE05	810	0.71	0.59	6.11	0.53	55.6
	UE06	990*	0.70	0.58	6.03	0.09	58.9
W 3% Re, Rolled	410F	930*	0.68	3.20	10.1	0.26	35.9
K-doped W 3% Re, Recrystallized	700F	980*	0.69	3.20	10.6	0.37	33.7
K-doped W 3% Re, Rolled	800F	920*	0.68	3.20	11.0	0.44	32.7

294   *Denotes best estimate of temperature*
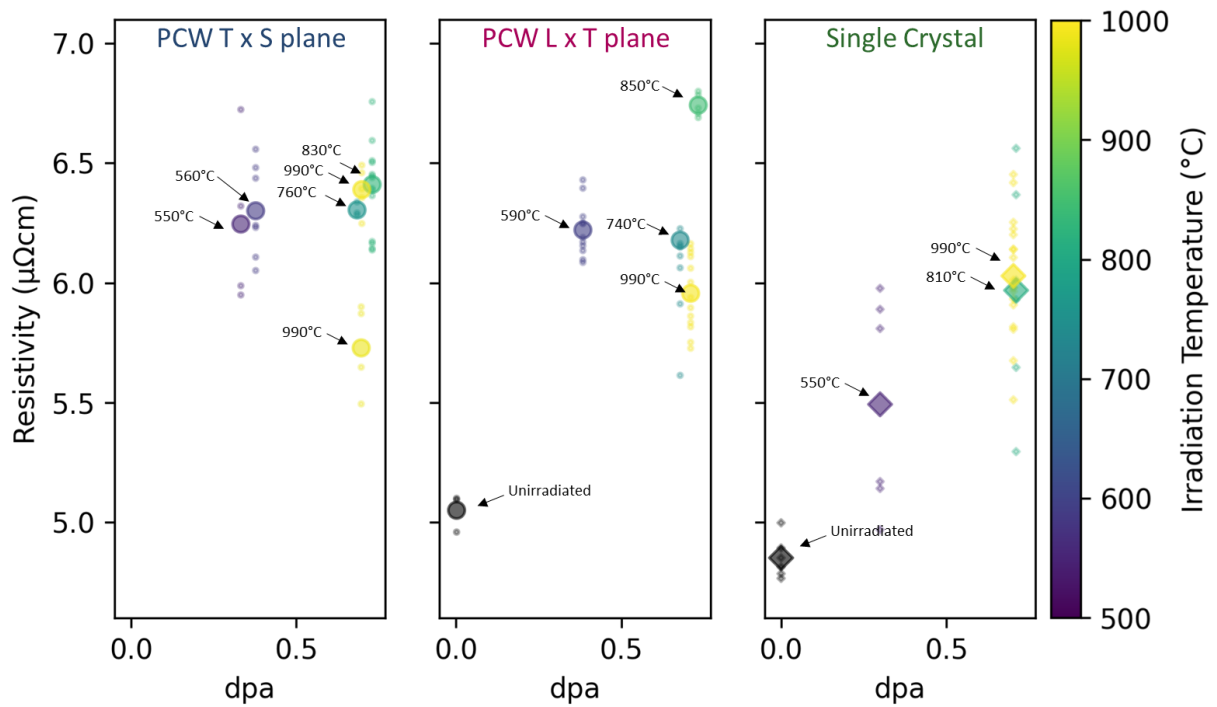
296   *Figure 6. Resistivity as a function of dose and irradiation temperature for SCW and PCW samples. Large markers denote mean*
297   *values; small markers are individual measurements.*

298   3.2.1   Thermal Diffusivity
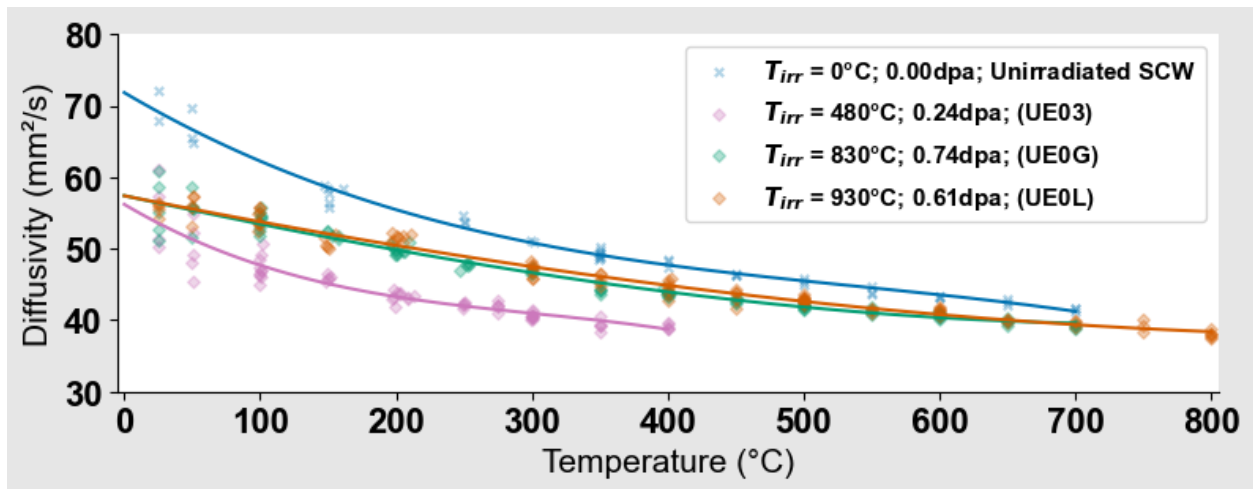
299

300   *Figure 7. Measured thermal diffusivity data (with fits) for SCW samples.*

301   Thermal diffusivity measurements of SCW specimens, with third-order polynomial fits, are shown in

302   Figure 7. Specimens are half tensile bars from the same irradiation capsules, but different areas of these

303   capsules. Therefore, irradiation conditions are similar, but not identical to, the electrical resistivity

304   specimens. No hysteresis was observed in any of the samples, so it is assumed that the measurement

305   temperature never exceeded the maximum irradiation temperature. Comparing the samples irradiated

306   at 830°C and 930°C, which have similar dose levels, we can note that there is minimal diffusivity

307   difference. We can conclude from this that there is little temperature effect between these

308   temperatures. The low-temperature irradiation - at significantly less dose - exhibits markedly less

309   diffusivity compared to the high temperature irradiations.

4   Discussion

311   To model the total resistivity of irradiated tungsten, we should consider lattice resistivity ($\rho_{lattice}$) plus the

312   effects of GBs (ρ_{GB}), solid-solution transmutation ($\rho_{tr.SS}$), transmutant precipitates in the bulk ($\rho_{tr.P}$),

313   transmutant segregation to GBs ($\rho_{tr.GB}$), voids (ρ_{void}), dislocations (ρ_{dis}), vacancies (ρ_v), interstitials (ρ_i),

314   and crystallographic texture (ρ_{tex}). According to Matthiessen's approximation rule for electrical

315   resistivity, the total resistivity of a crystalline metallic material can be represented as the sum of the

316   lattice resistivity and these imperfections to the lattice. In the most general form for this situation:

317   *Equation 5:*

318   $$\rho_{total} = \rho_{lattice} + \rho_{GB} + \rho_{tr.SS} + \rho_{tr.P} + \rho_{tr.GB} + \rho_{void} + \rho_{dis} + \rho_v + \rho_i + \rho_{tex}$$

319   Mergia et al[39] and Reza et al [40] provide two recent discussions focusing on void, vacancy, and

320   dislocation effects in irradiated tungsten. Here, we will seek to discuss and expand the understanding of

321   the changes attributable to GBs, transmutation/Re content, and textural effects. To build necessary

322   context, we will also discuss effects associated with irradiation temperature and evaluate whether the

323   Wiedemann–Franz law holds under irradiation.

4.1   Temperature effects

325   Recovery of irradiation effects in metals generally follows four distinct stages[11–13]. In tungsten, stage

326   III (self-interstitial migration) is divided into two separate regions, the first between 100-450°C, and the

327   second between 450-650°C. Stage IV (vacancy migration) occurs between 650-1000°C. Keyes and

328   Moteff's [11] work shows the relative effect (at doses between $8.5 \bullet 10^{17}$ and $1.5 \bullet 10^{21}$ n/cm^2) of each

329   of these recovery stages to be stage III (1) as the most degrading to resistivity, then stage IV, then stage

330   III (2). All materials discussed here were irradiated beyond the first self-interstitial region, and within

331   the second, but not all fell inside the region for vacancy migration. Vacancy density, therefore, is

332   believed to contribute significantly to the resistivity between the low and high temperature samples,

333   while self-interstitials are not. In this context, the high resistivity/low diffusivity of the low-

334   temperature/low dose specimens, when compared to the high temperature/high dose cases, can be

335   understood.

4.2 Comparison between resistivity and diffusivity

Table 6 shows a comparison of calculated electronic contribution to thermal diffusivity from this work alongside fits from measured thermal diffusivity values. Akiyoshi et al.'s[34] measurements are from material from the same irradiation and same parent block of material as the A/B/C orientation specimens. In unirradiated specimens, they note a difference of 3 mm^2/s ($\approx$5%) in thermal diffusivity, depending on grain orientation – reasonably similar to our calculated difference of 2.3 mm^2/s for unirradiated B-orientation material. Generally, the unirradiated and irradiated specimens exhibit similar diffusivity whether calculated from resistivity measurements or measured directly. Dose and temperature differences, however, make exact comparison difficult. It should also be noted that laser flash method should expect ~5% error at room temperature [41].

Table 6. Comparison of measured/fitted thermal diffusivity values, α, and electronic contribution to the thermal diffusivity, α_e calculated with a Lorenz number of 3.2 • 10^{-8} WΩK^{-2}. Uncertainty given in α_e is one standard deviation. Data attributed to Akiyoshi can be found in [34]. Orientation defines whether elongated grains are perpendicular or parallel to the direction of heat/electron flow.

Sample ID	Dose (dpa)	Irrad. Temp (°C)	Orientation	Measurement fit α at room temp (mm^2/s)	Calculated α_e at 20°C (mm^2/s)	Reference
BT no irrad	0	-	⊥		69.5±2.1	Present work
4003	0	-	⊥	70.8		[34]
BT no irrad	0	-	//		71.8±1.9	Present work
500H	0	-	//	73.8		[34]
BT02	0.38	590	⊥		55.2±2.1	Present work
4000	0.46	660	⊥	58.0		[34]
BT02	0.38	590	//		58.3±2.0	Present work
5001	0.25	550	//	58.5		[34]
Sample ID	**Dose (dpa)**	**Irrad. Temp (°C)**	**Orientation**	**Measurement fit α at 20°C (mm^2/s)**	**Calculated α_e at 20°C (mm^2/s)**	**Reference**
UE no irrad	0	-	-		74.7±2.4	Present work
UE no irrad 2	0	-	-	69.7		Present work
UE02	0.30	550	-		66.0±9.8	Present work
UE03	0.26	480	-	54.0		Present work
UE05	0.71	810	-		55.6±8.6	Present work
UE0G	0.74	830	-	55.6		Present work
UE06	0.70	990	-		58.9±1.8	Present work
UE0L	0.63	930	-	55.6		Present work

350

351 Comparing SCW data from this work, we see reasonably similar values between doses and temperatures

352 between the measured and fitted α and the calculated α_e. The only exception to this is in the low-

353 temperature, low-dose instance. Here, the calculated α_e is much higher than measured α. We attribute

354 this discrepancy to either the lower irradiation temperature of UE03 (and therefore the effect of Frenkel

355 pairs creating some deviation from Wiedemann-Franz) or the particularly large data spread for the

356 resistivity of this sample (see Figure 6). Because we find such similarity between measured α and

357 calculated α_e, for similar doses on identical materials, we cannot show any systematic deviation from

358 Wiedemann–Franz. Therefore, we assume that Wiedemann–Franz holds for neutron-irradiated

359 tungsten at the measured doses/temperatures.

360 ## 4.3   Effect of Rhenium content

361 Electrical resistivity evolution in neutron irradiated tungsten has been recently studied by Tanno et al.

362 [42] (≤1.54dpa, ≤740°C, irradiated in the Joyo fast reactor), Hasegawa et al. [15] (0.15–1.0 dpa at around

363 500–600 °C) , and Mergia et al. [29] (0.18dpa, ≤1200°C, irradiated with steel shielding in the fuel

364 element of BR2). The change in resistivity (induced either by addition of Re during alloying (other

365 authors) or neutron irradiation in HFIR (present work)) is plotted against reported dpa for similar

366 temperatures in Figure 8. A single pre-alloyed, irradiated sample - 410F (W3%Re, shown in orange)

367 measures the changed resistivity against unalloyed, unirradiated PCW – effectively adding both

368 irradiation and alloying effects.

369 Resistivity contributions from transmutation impurities in solid solution can be calculated using

370 Matthiessen's rule with Tanno's[42] calculated impurity parameters, I, and the impurity content, x, in %

371 at. This parameter can be calculated separately for each constituent, but is only done for Re in this work

372 using Tanno's impurity parameter of 145 for Re in W.

373   *Equation 6:*

374
$$\rho_{tr.SS} = Ix(1-x)$$
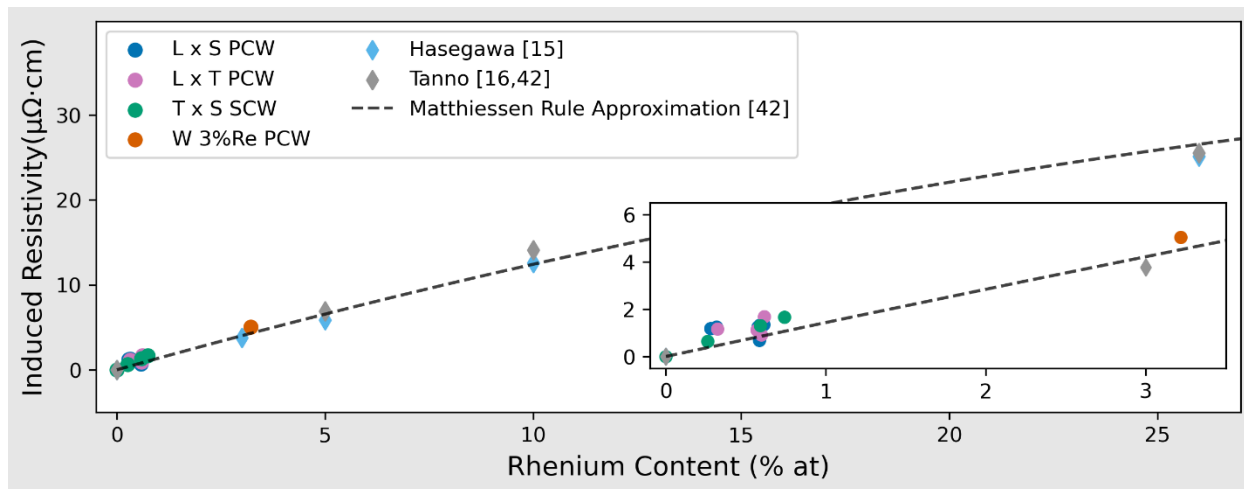
375

376   *Figure 8. Comparison of recent resistivity/neutron irradiation studies with this work. Work from Tanno et al.[16,42] and*

377   *Hasegawa et al.[15] are for unirradiated material. The fit dashed line displayed is derived from Tanno's calculations of impurity*

378   *parameters for Matthiessen's rule.*

379   In neutron irradiated tungsten (both in samples from this irradiation and elsewhere) [36,43],

380   transmutant Re precipitates at the grain boundaries. In SCW samples, and far from grain boundaries, Re

381   (and Os) precipitate into clusters at sufficient dose, rather than remaining in solid solution.

382   From the TEM data on samples from this irradiation campaign, we know that the highest-dose SCW

383   samples experience concentration of transmutant elements around voids, while the PCW specimens do

384   not exhibit this behavior at the same levels, but may experience segregation to the GBs. We posit,

385   therefore, that our PCW samples exhibit transmutation effects which cause increases in resistivity due

386   to lattice changes from solid-solution and GBs but not precipitates, while the SCW samples exhibit

387   transmutant solid solution and precipitation effects, but not GBs.

388   ## 4.4   Grain Boundary and Matrix Resistivity

389   Resistivity as a function of GB density – in the direction of the current – is shown in in Figure 9 A) for

390   three samples with elongated grains which were rotated to achieve different GB densities (see the top

391   row of Figure 5). GBs present a natural scattering site for electrons. In addition, studies have

392   shown[37,44], Re enrichment will occur at GBs in irradiated W. Any such enrichment necessitates

393   electrons cross a Re-enriched zone, while Re pre-clusters and clusters may be bypassed elsewhere and

394   in SCW. Assuming the effect of grain boundaries scales linearly with GB density, the slope of the line in

395   Figure 9 A) can be taken as the GB effect on resistivity. There is an observed increasing slope trend

396   (from 0.4 to 0.6 $\frac{\mu\Omega \cdot cm}{GB/\mu m}$ per at% Re) with increasing dose/Re content. The uncertainty thresholds in

397   resistivity, however, make this trend difficult to quantify precisely and would benefit from future study.
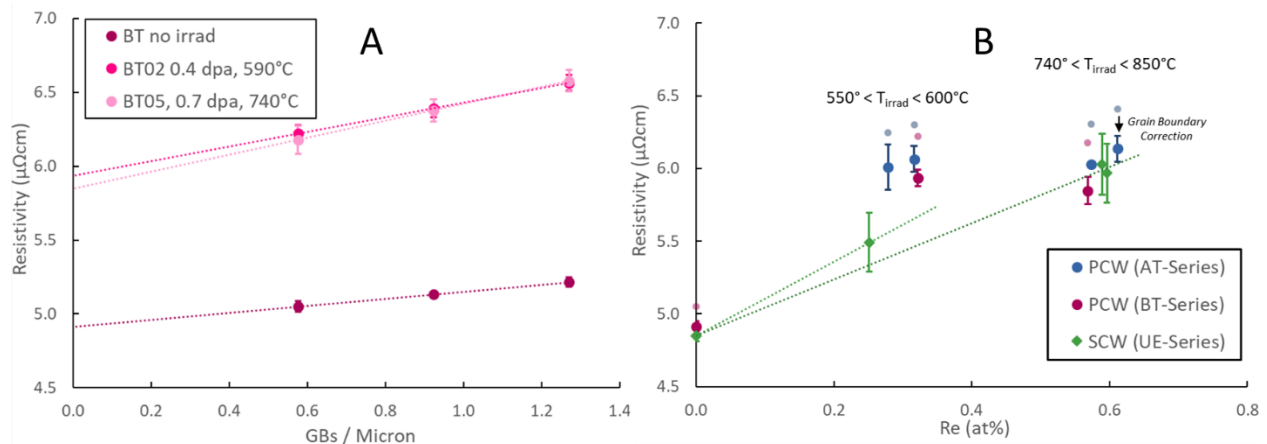
398

399   *Figure 9. A) Resistivity for oscillatory BT-series samples as a function of GB density. B) PCW resistivity values minus the*
400   *calculated GB effect from part A are compared with SCW. Original, as-measured PCW shown with smaller, lighter markers.*
401   *Uncertainty bars are standard deviation.*

402   From the discussion in 4.4, we suspect that the degradation of the GB effects in PCW is due to

403   segregation of Re to the GBs. We, therefore, attribute the changes to the resistivity slope to Re

404   segregation to the GBs.

405   We can build an expression for grain boundary resistivity from work performed by Andrews et al.

406   [45,46], which has recently been explored in conjunction with Matthiessen's rule by Bakonyi [47].

407   Andrews et al.'s work assumes spherical grains, however, which are not the case for this work.

408   Geometrically, we assume that all grains can be treated as ellipsoids with perpendicular radii of a, b, and

409   c in the x, y, and z axes, respectively. We define the direction of the current to be in the z-direction.

410   Considering only net electron motion in the direction of the current, the mean distance encountered

411   between grain boundary encounters will be the average height, z, of the ellipsoid. Which can be derived

412   by doubling the mean chord length of the positive octant of an ellipsoid centered on the origin, where A

413   represents the cross-sectional area of the ellipse in the x-y plane.

414   *Equation 7:*

415
$$Mean(z) = 2 \cdot \frac{1}{\frac{1}{4}A} \iint z(x,y)dydx = 2 \cdot \frac{1}{\frac{1}{4}A} \int_0^a \int_0^{b\sqrt{1-\frac{x^2}{a^2}}} c\sqrt{1 - \frac{x^2}{a^2} - \frac{y^2}{b^2}}\ dy\ dx = \frac{4}{3}c$$

416   Conveniently, this is the same result as the spherical case explored by Andrews et al. [46]. Therefore, we

417   can proceed to approximate GB resistivity effects with the simple expression:

418   *Equation 8:*

419
$$\rho_{GB} + \rho_{tr.GB} = \frac{A}{d}$$

420   Here, *d* is the diameter of the grain in the direction of the current, (replacing c, which was used above,

421   for an easier to understand convention) and *A* is the Andrews parameter (a proportionality factor equal

422   to the slope of the lines in Figure 9A). Resistivity attributed to GBs and calculated values for A are

423   shown alongside calculated Re content and extrapolated resistivity for the zero-GB condition in Table 7.

424   *Table 7. Irradiation condition, resistivity range attributed to GB effects, Andres Parameter, calculated Re content, and calculated*
425   *zero-GB resistivities for selected samples.*

Irradiation Condition	ρ_{GB} ($\Delta\rho_{GB}$) ($\mu\Omega\bullet$cm)	Relative effect	Andrews Parameter ($\mu\Omega\bullet$cm/GB/μm)	Calculated Re (at%)	Zero-GB ρ ($\mu\Omega\bullet$cm)

SCW no irradiation	-	-	-	-	4.9
L x T no irradiation	0.14-0.30 (0.17)	3.2%	0.24	0	4.9
L x T 0.4 dpa / 590°C	0.28-0.63 (0.34)	5.2%	0.49	0.4%	5.9
L x T 0.7 dpa / 740°C	0.33-0.73 (0.40)	6.1%	0.58	0.8%	5.8

426

427 When considering the matrix effects observed in Figure 9 B), we note good agreement between the

428 calculated matrix resistivity from PCW samples and observed resistivity from the SCW samples. The only

429 exception to this is in the 550-600°C irradiations, where the SCW samples appear to have lower

430 resistivity than the calculated matrix values. It is unclear what this is attributable to. Two possible

431 explanations include: 1) the fact that we only have a single SCW sample, which itself has a large

432 uncertainty, gives a misleading impression or 2) GBs inhibiting self-interstitial migration to a greater

433 degree than acting as an interstitial sink.

434 ## 4.5 Textural effects

435   Textural effects could provide an alternate explanation for the observed oscillatory effects in

436 measurements. Zakharova et al. [17] reported electrical resistivity values for SCW, measured at 25°C,

437 for the [100], [110], and [111] directions. The samples were measured again after neutron irradiation at

438 460°C in BR-10 to fluences of 1.14×10^{26} n/m^2 (E > 0.1 MeV) – roughly triple the highest dose from this

439 work of 0.37×10^{26} n/m^2 (E > 0.1 MeV). Their results, reproduced in Table 8, indicate a maximum

440 textural difference of 0.07 μΩ•cm before irradiation and 0.24 μΩ•cm after irradiation.

441 *Table 8. SCW orientation effects reported by Zakharova et al.* [17]

	[100]	[110]	[111]	Max Difference	Relative effect
Unirr ρ (μΩ•cm)	5.62	5.55	5.62	0.07	1.2%
Irr @ 900°C ρ (μΩ•cm)	6.57	6.33	6.38	0.24	3.7%
Irr @ 900°C Annealed ρ (μΩ•cm)	6.45	6.30	6.33	0.15	2.3%

442

443   Because we would expect texture to have - at absolute maximum - an effect of 3.7%, observe oscillatory

444   effects as high as 6.1%, and do not observe oscillation in the rotation of SCW samples (to within our

445   measurement limits), we do not find texture to be an adequate explanation to observed oscillation.

446   4.6   Attribution of specific irradiation effects on resistivity degradation
447

448   From Equation 5, we have been able to measure or estimate values for lattice resistivity ($\rho_{lattice}$), the

449   effects of GBs (ρ_{GB}) together with transmutant segregation to GBs ($\rho_{tr.GB}$), and solid-solution

450   transmutation ($\rho_{tr.SS}$). For our dose and temperature regime, we observe no evidence of transmutant

451   precipitates in the bulk ($\rho_{tr.P}$) and assume no significant textural effects (ρ_{tex}). Void (ρ_{void}), dislocation

452   (ρ_{dis}), vacancy (ρ_v), and interstitial effects (ρ_i) are at least partially annealed out at the highest

453   temperature irradiations. Therefore, the sum of these four effects should be inversely proportional to

454   irradiation temperature and proportional to dose until/unless saturation of defects occurs. This sum

455   (termed ρ_{temp} for the inverse relationship to irradiation temperature) can be quantified by subtracting

456   the quantified effects from the observed resistivity ($\rho_{observed}$). Calculated values are show in Table 9.

457   *Equation 9:*

458   $$\rho_{temp} = \rho_{void} + \rho_{dis} + \rho_v + \rho_i = \rho_{observed} - \rho_{lattice} - \rho_{GB} - \rho_{tr.SS} - \rho_{tr.GB}$$

459   *Table 9. Calculated resistivity contributions to observed resistivity. L x T face samples use directly calculated Andrews*
460   *parameters. GB contributions for L x S face samples irradiated at similar conditions are calculated with identical Andrews*
461   *parameters. Resistivity values are $\mu\Omega \cdot cm$*

Irradiation Condition	Sample ID	Re (% at)	$\rho_{observed}$	$\rho_{lattice}$	$\rho_{GB} + \rho_{tr.GB}$	$\rho_{tr.SS}$	ρ_{temp}
SCW no irradiation	UEnorad	-	4.85	4.85	-	-	-
SCW 0.3 dpa / 480°C	UE02	0.26%	5.49	4.85	-	0.38	0.27
SCW 0.7 dpa / 830°C	UE05	0.74%	5.97	4.85	-	1.07	0.05
L x T no irradiation	BTnorad	-	5.05	4.85	0.14	-	-
L x T 0.4 dpa / 590°C	BT02	0.32%	6.22	4.85	0.28	0.47	0.62
L x T 0.7 dpa / 740°C	BT05	0.57%	6.18	4.85	0.33	0.82	0.18
L x S 0.4 dpa / 590°C	AT01	0.32%	6.30	4.85	0.24	0.46	0.76
L x S 0.7 dpa / 760°C	AT05	0.57%	6.30	4.85	0.27	0.83	0.35

462

463   We conclude from these calculations that – for the polycrystalline samples – the combined resistivity

464   degradation from voids, dislocations, vacancies, and interstitials is likely greater than that from solid

465   state transmutation at lower (~590°C) irradiation temperatures. This trend reverses at higher

466   temperature irradiation, where mobile lattice defects can anneal out, and the solid solution

467   transmutation becomes the dominant factor at higher temperatures (shown here in the temperatures

468   ≥740°C).

469

470   5   Summary and Conclusions

471   Electrical resistivity and thermal diffusivity measurements have been taken for neutron irradiated W and

472   W-3%Re with Re transmutation rates similar to what is expected in fusion reactors. Materials were

473   irradiated to doses between 0.3 – 0.9 dpa at temperatures ranging from 550 – 990°C and changes to

474   resistivity have been reported. Based on the literature, a mathematical description of irradiation effects

475   on electron transport has been presented. We conclude that:

476   • Electrical resistivity varies with grain boundary density in respect to the direction of the applied

477   current. This variation has been quantified with respect to grain size. Andrews parameters

478   (which can be used to calculate grain boundary contributions for arbitrary grain sizes) have been

479   calculated for unirradiated W and W irradiated at these conditions. Increasing irradiation dose

480   appears to increase the Andrews parameter.

481   • For samples irradiated to 0.4 dpa near 590°C (below the vacancy migration threshold around

482   650°C), the combined resistivity degradation due to voids, vacancies, interstitials, and

483   dislocations is estimated to be greater than the contribution from solid solution Re

484   transmutation, which in turn is greater than the contribution from grain boundaries. At doses

485   0.7 dpa near 750°C, solid solution Re contributions to resistivity degradation are greater than all

486   other effects combined. In the no-irradiation case and doses/temperatures near 0.7 dpa /

487   750°C, observed SCW resistivity and the adjusted PCW matrix resistivity with these Andrews

488   parameters are similar.

489   • Based on thermal diffusivity and electrical resistivity data, the Wiedemann–Franz law appears to

490   hold for tungsten under irradiation for the measured conditions.

491   • Grain growth has been observed and quantified for our irradiation conditions – mean aerial

492   growth rates of 0.5 μm^2 (550°C/0.29 dpa) and 1.2 μm^2 (870°C/0.74 dpa) for the tested

493   microstructure. Recrystallization has also been observed in high temperature (~990°C)

494   irradiations.

6 Acknowledgements

7 References

506 [1]   A.F. Rowcliffe, L.M. Garrison, Y. Yamamoto, L. Tan, Y. Katoh, Materials challenges for the fusion
507   nuclear science facility, Fusion Engineering and Design. 135 (2018) 290–301.
508   https://doi.org/10.1016/j.fusengdes.2017.07.012.

509 [2] C.E. Kessel, J.P. Blanchard, A. Davis, L. El-Guebaly, L.M. Garrison, N.M. Ghoniem, P.W.
510 Humrickhouse, Y. Huang, Y. Katoh, A. Khodak, E.P. Marriott, S. Malang, N.B. Morley, G.H. Neilson,
511 J. Rapp, M.E. Rensink, T.D. Rognlien, A.F. Rowcliffe, S. Smolentsev, L.L. Snead, M.S. Tillack, P.
512 Titus, L.M. Waganer, G.M. Wallace, S.J. Wukitch, A. Ying, K. Young, Y. Zhai, Overview of the fusion
513 nuclear science facility, a credible break-in step on the path to fusion energy, Fusion Engineering
514 and Design. 135 (2018) 236–270. https://doi.org/10.1016/j.fusengdes.2017.05.081.

515 [3] Y. Chen, J. Ma, W. Li, Understanding the thermal conductivity and Lorenz number in tungsten
516 from first principles, Physical Review B. 99 (2019). https://doi.org/10.1103/PhysRevB.99.020305.

517 [4] J.-P. Crocombette, P. Notargiacomo, M.-C. Marinica, Effect of the variation of the electronic
518 density of states of zirconium and tungsten on their respective thermal conductivity evolution
519 with temperature, Journal of Physics: Condensed Matter. 27 (2015) 165501.
520 https://doi.org/10.1088/0953-8984/27/16/165501.

521 [5] L. Hu, B.D. Wirth, D. Maroudas, Thermal conductivity of tungsten: Effects of plasma-related
522 structural defects from molecular-dynamics simulations, Applied Physics Letters. 111 (2017)
523 081902. https://doi.org/10.1063/1.4986956.

524 [6] B. Fu, W. Lai, Y. Yuan, H. Xu, W. Liu, Calculation and analysis of lattice thermal conductivity in
525 tungsten by molecular dynamics, Journal of Nuclear Materials. 427 (2012) 268–273.
526 https://doi.org/10.1016/j.jnucmat.2012.05.015.

527 [7] T. Tanabe, C. Eamchotchawalit, C. Busabok, S. Taweethavorn, M. Fujitsuka, T. Shikama,
528 Temperature dependence of thermal conductivity in W and W–Re alloys from 300 to 1000 K,
529 Materials Letters. 57 (2003). https://doi.org/10.1016/S0167-577X(02)01403-9.

530 [8] B. Fu, W. Lai, Y. Yuan, H. Xu, W. Liu, Calculation and analysis of lattice thermal conductivity in
531 tungsten by molecular dynamics, Journal of Nuclear Materials. 427 (2012).
532 https://doi.org/10.1016/j.jnucmat.2012.05.015.

533 [9] J.A.H. Littleton, R.A. Secco, W. Yong, M. Berrada, Electrical resistivity and thermal conductivity of
534 W and Re up to 5 GPa and 2300 K, Journal of Applied Physics. 125 (2019).
535 https://doi.org/10.1063/1.5066103.

536 [10] Y. Katoh, L.L. Snead, L.M. Garrison, X. Hu, T. Koyanagi, C.M. Parish, P.D. Edmondson, M. Fukuda,
537 T. Hwang, T. Tanaka, A. Hasegawa, Response of unalloyed tungsten to mixed spectrum neutrons,
538 Journal of Nuclear Materials. 520 (2019) 193–207.
539 https://doi.org/10.1016/j.jnucmat.2019.03.045.

540 [11] L.K. Keys, J.P. Smith, J. Moteff, High-Temperature Recovery of Tungsten after Neutron Irradiation,
541 Physical Review. 176 (1968). https://doi.org/10.1103/PhysRev.176.851.

542 [12] H.H. Neely, D.W. Keefer, A. Sosin, Electron Irradiation and Recovery of Tungsten, Physica Status
543 Solidi (b). 28 (1968). https://doi.org/10.1002/pssb.19680280225.

544 [13] M.W. Thompson, The damage and recovery of neutron irradiated tungsten, Philosophical
545 Magazine. 5 (1960) 278–296. https://doi.org/10.1080/14786436008235842.

546 [14] M.S. Anand., B.M. Pande, R.P. Agarwala, Recovery in neutron irradiated tungsten, Radiat Eff. 39
547   (1978) 149–155. https://doi.org/10.1080/00337577808234468.

548 [15] A. Hasegawa, T. Tanno, S. Nogami, M. Satou, Property change mechanism in tungsten under
549   neutron irradiation in various reactors, in: Journal of Nuclear Materials, 2011: pp. 491–494.
550   https://doi.org/10.1016/j.jnucmat.2010.12.114.

551 [16] T. Tanno, A. Hasegawa, M. Fujiwara, J.C. He, S. Nogami, M. Satou, T. Shishido, K. Abe,
552   Precipitation of solid transmutation elements in irradiated tungsten alloys, Materials
553   Transactions. 49 (2008) 2259–2264. https://doi.org/10.2320/matertrans.MAW200821.

554 [17] M.I. Zakharova, N.A. Artemov, V. v. Bogdanov, Effects of Neutron Irradiation and Annealing on
555   the Elastic Moduli and Electrical Resistivity of Molybdenum and Tungsten Single Crystals,
556   Inorganic Materials. 37 (2001) 786–789. https://doi.org/10.1023/A:1017979230262.

557 [18] Y. Katoh, D. Clark, Y. Ueda, Y. Hatano, M. Yoda, A.S. Sabau, T. Yokomine, L.M. Garrison, J.W.
558   Geringer, A. Hasegawa, T. Hinoki, M. Shimada, D. Buchenauer, Y. Oya, T. Muroga, Progress in the
559   U.S./Japan PHENIX project for the technological assessment of plasma facing components for
560   DEMO reactors, Fusion Science and Technology. 72 (2017) 222–232.
561   https://doi.org/10.1080/15361055.2017.1333868.

562 [19] J.W. Geringer, J.L. McDuffee, C.M. Petrie, L.M. Garrison, R.H. Howard, N.O. Cetiner, D.A.
563   Stringfield, R.G. Sitterson, 10.4 HFIR-MFE-RB-19J Specimen Loading Listing, 2016.

564 [20] L.M. Garrison, Y. Katoh, N. Reid, E. Proehl, M. Fukuda, 4.6 MICROSTRUCTURE AND MECHANICAL
565   PROPERTIES OF IRRADIATED PHENIX PROGRAM TUNGSTEN, 2017.

566 [21] M.E. Sawan, Transmutation of Tungsten in Fusion and Fission Nuclear Environments, Fusion
567   Science and Technology. 66 (2014). https://doi.org/10.13182/FST13-717.

568 [22] T. Noda, M. Fujita, M. Okada, Transmutation and induced radioactivity of W in the armor and
569   first wall of fusion reactors, Journal of Nuclear Materials. 258–263 (1998).
570   https://doi.org/10.1016/S0022-3115(98)00088-9.

571 [23] L.M. Garrison, Y. Katoh, J.W. Geringer, M. Akiyoshi, X. Chen, M. Fukuda, A. Hasegawa, T. Hinoki,
572   X. Hu, T. Koyanagi, E. Lang, M. McAlister, J. McDuffee, T. Miyazawa, C. Parish, E. Proehl, N. Reid, J.
573   Robertson, H. Wang, PHENIX U.S.-Japan Collaboration Investigation of Thermal and Mechanical
574   Properties of Thermal Neutron–Shielded Irradiated Tungsten, Fusion Science and Technology. 75
575   (2019). https://doi.org/10.1080/15361055.2019.1602390.

576 [24] L.R. Greenwood, B.D. Pierson, T. Trang-Le, 11.4 HFIR-MFE-RB-19J NEUTRON FLUENCE
577   MEASUREMENTS AND RADIATION DAMAGE CALCULATIONS (REVISED), 2019.

578 [25] T. Noda, M. Fujita, M. Okada, Transmutation and induced radioactivity of W in the armor and
579   first wall of fusion reactors, Journal of Nuclear Materials. 258–263 (1998).
580   https://doi.org/10.1016/S0022-3115(98)00088-9.

581 [26] M.E. Sawan, Transmutation of Tungsten in Fusion and Fission Nuclear Environments, Fusion
582   Science and Technology. 66 (2014). https://doi.org/10.13182/FST13-717.

583 [27] J. L. McDuffee, C. R. Daily, N. O. Cetiner, C. M. Petrie, J. W. Geringer, 10.3 HFIR-MFE-RB-19J
584   Thermal and Neutronic Design, 2016.

585 [28] J.-H. You, M. Li, K. Zhang, Structural lifetime assessment for the DEMO divertor targets: Design-
586   by-analysis approach and outstanding issues, Fusion Engineering and Design. 164 (2021) 112203.
587   https://doi.org/10.1016/j.fusengdes.2020.112203.

588 [29] J.P. Blanchard, C. Martin, Thermomechanical Analysis for an All-Tungsten ARIES Divertor, Fusion
589   Science and Technology. 67 (2015) 158–166. https://doi.org/10.13182/FST14-796.

590 [30] J. McDuffee, T. Daly, Experimental and Computational Study of the Flux Spectrum in Materials
591   Irradiation Facilities of the High Flux Isotope Reactor, in: PHYSOR 2012 - Advances in Reactor
592   Physics - Linking Research, Industry, and Education, 2012.

593 [31] A.A. Campbell, W.D. Porter, Y. Katoh, L.L. Snead, Method for analyzing passive silicon carbide
594   thermometry with a continuous dilatometer to determine irradiation temperature, Nuclear
595   Instruments and Methods in Physics Research Section B: Beam Interactions with Materials and
596   Atoms. 370 (2016). https://doi.org/10.1016/j.nimb.2016.01.005.

597 [32] M.A. Logan, An AC Bridge for Semiconductor Resistivity Measurements Using a Four-Point Probe,
598   1961.

599 [33] ASTM B193-20: Standard Test Method for Resistivity of Electrical Conductor Materials, ASTM
600   International. (2020).

601 [34] M. Akiyoshi, L.M. Garrison, J.W. Geringer, H. Wang, A. Hasegawa, S. Nogami, Y. Katoh, Thermal
602   diffusivity of irradiated tungsten and tungsten-rhenium alloys, Journal of Nuclear Materials. 543
603   (2021). https://doi.org/10.1016/j.jnucmat.2020.152594.

604 [35] W. Pantleon, Thermal stability of the microstructure in rolled tungsten for fusion reactors,
605   Physica Scripta. 96 (2021) 124036. https://doi.org/10.1088/1402-4896/ac2854.

606 [36] X. Hu, C.M. Parish, K. Wang, T. Koyanagi, B.P. Eftink, Y. Katoh, Transmutation-induced
607   precipitation in tungsten irradiated with a mixed energy neutron spectrum, Acta Materialia. 165
608   (2019) 51–61. https://doi.org/10.1016/j.actamat.2018.11.032.

609 [37] T. Koyanagi, N.A.P.K. Kumar, T. Hwang, L.M. Garrison, X. Hu, L.L. Snead, Y. Katoh, Microstructural
610   evolution of pure tungsten neutron irradiated with a mixed energy spectrum, Journal of Nuclear
611   Materials. 490 (2017) 66–74. https://doi.org/10.1016/j.jnucmat.2017.04.010.

612 [38] L.M. Garrison, Y. Katoh, N.A.P.K. Kumar, Mechanical properties of single-crystal tungsten
613   irradiated in a mixed spectrum fission reactor, Journal of Nuclear Materials. 518 (2019).
614   https://doi.org/10.1016/j.jnucmat.2019.02.050.

615 [39] K. Mergia, V. Chatzikos, E. Manios, S. Dellis, D. Papadakis, D. Terentyev, G. Bonny, A. Dubinko, I.E.
616   Stamatelatos, S. Messoloras, M. Rieth, Evolution of microstructure in neutron irradiated cold
617   rolled tungsten and its correlation with hardness, Fusion Engineering and Design. 172 (2021)
618   112784. https://doi.org/10.1016/j.fusengdes.2021.112784.

619   [40]   A. Reza, H. Yu, K. Mizohata, F. Hofmann, Thermal diffusivity degradation and point defect density
620   in self-ion implanted tungsten, Acta Materialia. 193 (2020) 270–279.
621   https://doi.org/10.1016/j.actamat.2020.03.034.

622   [41]   ASTM E1461-13: Standard Test Method for Thermal Diffusivity by the Flash Method, 2016.

623   [42]   T. Tanno, A. Hasegawa, J.C. He, M. Fujiwara, M. Satou, S. Nogami, K. Abe, T. Shishido, Effects of
624   transmutation elements on the microstructural evolution and electrical resistivity of neutron-
625   irradiated tungsten, Journal of Nuclear Materials. 386–388 (2009) 218–221.
626   https://doi.org/10.1016/j.jnucmat.2008.12.091.

627   [43]   R.K. Williams, F.W. Wiffen, J. Bentley, J.O. Stiegler, Irradiation induced precipitation in tungsten
628   based, W-Re alloys, Metallurgical Transactions A. 14 (1983) 655–666.
629   https://doi.org/10.1007/BF02643781.

630   [44]   M. Dürrschnabel, M. Klimenkov, U. Jäntsch, M. Rieth, H.C. Schneider, D. Terentyev, New insights
631   into microstructure of neutron-irradiated tungsten, Scientific Reports. 11 (2021) 7572.
632   https://doi.org/10.1038/s41598-021-86746-6.

633   [45]   P.V. Andrews, Resistivity due to grain boundaries in pure copper, Physics Letters. 19 (1965).
634   https://doi.org/10.1016/0031-9163(65)90776-6.

635   [46]   P. v. Andrews, M.B. West, C.R. Robeson, The effect of grain boundaries on the electrical
636   resistivity of polycrystalline copper and aluminium, Philosophical Magazine. 19 (1969).
637   https://doi.org/10.1080/14786436908225855.

638   [47]   I. Bakonyi, Accounting for the resistivity contribution of grain boundaries in metals: critical
639   analysis of reported experimental and theoretical data for Ni and Cu, The European Physical
640   Journal Plus. 136 (2021) 410. https://doi.org/10.1140/epjp/s13360-021-01303-4.

641
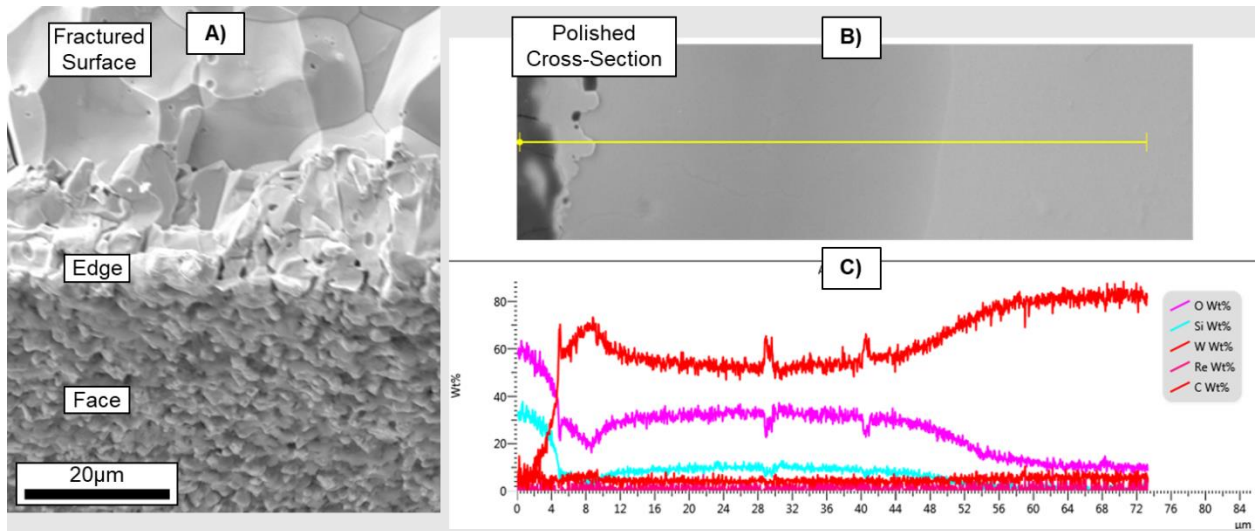
8   Supplemental Material

Supplemental Figure 1. A) Unpolished fracture surface and top face of a sample (BT07) which fractured during testing. Distinct differences are observed between the face, edge, and cross-section of the material. B) Polished cross-section and EDS line-scan indicating elevated oxygen content up to a depth of ~50μm for sample.
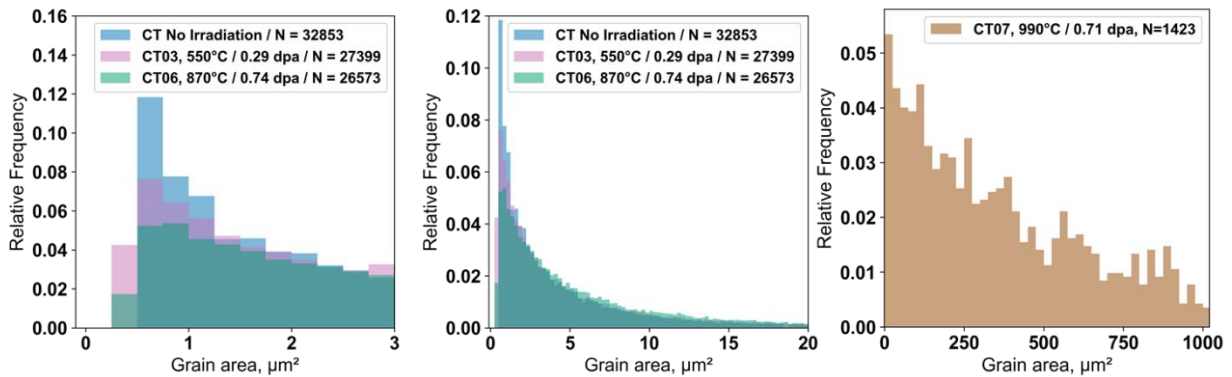
Supplemental Figure 2. Normalized histograms of grain area for 3 specimens at different irradiation conditions. Bin sizes are 0.25 μm², except for the rightmost plot, which uses bins of 25 μm².